

Author's accepted manuscript

Abdelgawwad, A., Catala, A. & Patzold, M. (2020). Doppler Power Characteristics Obtained from Calibrated Channel State Information for Human Activity Recognition. IEEE Vehicular Technology Conference. <https://doi.org/10.1109/VTC2020-Spring48590.2020.9129187>.

Published in: IEEE Vehicular Technology Conference

DOI: <https://doi.org/10.1109/VTC2020-Spring48590.2020.9129187>

AURA: <https://hdl.handle.net/11250/2735058>

Available online: 30/06/2020

© 2020 IEEE. Personal use of this material is permitted. Permission from IEEE must be obtained for all other uses, in any current or future media, including reprinting/republishing this material for advertising or promotional purposes, creating new collective works, for resale or redistribution to servers or lists, or reuse of any copyrighted component of this work in other works.

Doppler Power Characteristics Obtained from Calibrated Channel State Information for Human Activity Recognition

Ahmed Abdelgawwad¹, Andreu Català², and Matthias Pätzold¹

¹Faculty of Engineering and Science, University of Agder, P.O. Box 509, 4898 Grimstad,
Norway

²Universitat Politècnica de Catalunya (UPC), Rambla de l'Exposició, 59-69, 08800 Vilanova i
la Geltrú, Barcelona, Spain

E-mails: ¹{ahmed.abdel-gawwad, matthias.paetzold}@uia.no, ²andreu.catala@upc.edu

Abstract — This paper demonstrates the time-variant (TV) Doppler power characteristics of human activities using measured channel state information (CSI). We model the measured CSI as a complex channel transfer function corresponding to a 3D non-stationary multipath fading channel consisting of a fixed transmitter, a fixed receiver, fixed scatterers representing fixed objects, and a cluster of moving scatterers representing a moving person performing some human activities. We demonstrate the relationship between the TV Doppler frequency caused by each moving scatterer and the rate of change of its corresponding TV propagation delay. Furthermore, we express the TV mean Doppler shift in terms of the path gains of the fixed scatterers, the TV path gains, and the TV Doppler frequencies of the moving scatterers. To provide an insight into the TV Doppler power characteristics of the measured calibrated CSI, we employ the spectrogram from which we derive the TV mean Doppler shift. Finally, we present the spectrograms and the TV mean Doppler shifts of the measured calibrated CSI for different human activities. The results show the possibility of designing human activity recognition systems using commercial Wi-Fi devices by employing deep learning or machine learning algorithms.

Index Terms — Non-stationary, spectrogram, complex channel transfer function, TV Doppler power characteristics, CSI, human activity recognition.

D.1 Introduction

According to the statistics in [1], 28.7 % of the adults above 65 years have fall incidents. An increase in mortality and healthcare costs is a consequence of these fall incidents, especially for people aged 75 years or older. According to the United Nations' World Ageing Report [2], the number of adults over 60 is increasing. The number of adults over 80 is expected to rise from 137 million to 425 million between 2017 and 2050. As a result, it is expected that the demand for indoor human activity recognition (HAR) systems will increase. The main role of HAR systems is to distinguish between normal activities and dangerous activities such as falls. One of the types of HAR systems are radio-frequency-based (RF-based) non-wearable systems [3]. Such systems track human activities by using frequency-modulated carrier waves scattered by the major body segments, such as wrists, head, torso, and legs. These scattered waves contain the micro-Doppler characteristics caused by the moving body segments.

The time-variant (TV) compound Doppler effect caused by moving body segments (modelled for simplicity as a cluster of moving scatterers) has been incorporated in 3D channel models by taking into account the TV azimuth angle of motion (AAOM), the elevation angle of motion (EAOM), the azimuth angle of departure (AAOD), the elevation angle of departure (EAOD), the azimuth angle of arrival (AAOA), and the elevation angle of arrival (EAOA) in fixed-to-fixed (F2F) channel models. Such a phenomenon opened up the opportunity for many applications such as HAR [3, 4], detection of gait asymmetry [5], fall detection [6, 7], distinguishing between armed and unarmed humans for security [8], and gesture recognition [9]. Most of these applications are based on applying different machine learning, deep learning, or detection algorithms to the spectrograms of the measured multi-component radar signals. By employing the concept of the spectrogram, which is a time-frequency distribution, an insight into the TV Doppler power characteristics influenced by the moving body segments is revealed.

The authors of [10] introduced a software tool that can capture the channel state information (CSI). Such a tool operates according to the IEEE 802.11n standard [11] and collects data over 30 subcarriers operating in orthogonal-frequency-division-multiplexing (OFDM) mode. When it comes to processing the complex CSI data collected by this tool, one of the main challenges is that the transmitter and the receiver are not clock synchronized [12–14]. Consequently, the phases of the complex CSI data are highly distorted, which makes it impossible to explore the spectrograms of the complex CSI data. Attempts to overcome this issue have been proposed in [15, 16] by utilizing the principle component analysis or applying linear transformations on the distorted phases. However, these techniques do not contribute to the study of the true TV Doppler characteristics, since they partially or completely eliminate the true phases containing the Doppler shifts caused by the moving scatterers. The authors of [17] successfully eliminated the TV phase distortions by calibrating the transmitter and the receiver stations using a back-to-back (B2B) connection between them. They validated the

proposed method by measurements from a vector network analyzer. They tested the procedure by exploring the TV Doppler power characteristics of a simple hand gesture experiment and validated the results by simulation.

To the best of the authors' knowledge, no one has yet researched the TV Doppler power characteristics of measured calibrated CSI with B2B connection for human activities, such as walking, falling, etc. All the studies in the literature regarding the CSI were either on the amplitude or the distortion-eliminated phases through linear transformations. The main goal of this paper is to present some measurement results of calibrated CSI with B2B connection for some human activities. First, we model the channel transfer function (CTF) of a 3D non-stationary F2F channel and the TV Doppler frequencies caused by the moving scatterers. We elaborate on the relationship between the TV Doppler frequencies and the TV propagation delays. Then, we discuss the spectrogram of the presented channel model associated with each subcarrier and illustrate how the TV mean Doppler shift can be obtained from the spectrogram. Finally, we explore the spectrogram and the TV mean Doppler shift of the measured calibrated CSI for some human activities. The results of this paper are important for getting a better understanding of the influence of the channel parameters on the spectral characteristics of the channels in the presence of a moving person.

The rest of this paper is divided as follows. Section D.2 presents a model for the complex CTF and the TV Doppler shift caused by human activities. The spectrogram of the presented model and the computation of the TV mean Doppler shift from the spectrogram are discussed in Section D.3. Section D.4 demonstrates the measurement scenario, processing the CSI, the spectrogram of the measured CSI, and the analysis of the measured TV mean Doppler shift. Section D.5 gives concluding remarks and directions for future work.

D.2 Modelling the CTF

In this paper, we consider the scenario depicted in Fig. D.1. We have a fixed Wi-Fi transmitter T_x and a fixed Wi-Fi receiver R_x located at (x^T, y^T, z^T) and (x^R, y^R, z^R) , respectively. The scenario shows a moving person whose major body segments are modelled for simplicity by a cluster of \mathcal{N} moving point scatterers $S_{M,n}$ for $n = 1, 2, \dots, \mathcal{N}$. The fixed point scatterers $S_{F,m}$ ($m = 1, 2, \dots, \mathcal{M}$) in Fig. D.1 simply represent \mathcal{M} fixed objects such as walls, furniture, etc. Each moving point scatterer is characterized by its TV displacement $(x_{M,n}(t), y_{M,n}(t), z_{M,n}(t))$. The TV Euclidean distance between T_x (R_x) and the n th moving scatterer is denoted by $d_{M,n}^T(t)$ ($d_{M,n}^R(t)$). Single-bounce scattering is assumed, i.e., each wave launched from the T_x is scattered only once by either a fixed scatterer $S_{F,m}$ or a moving scatterer $S_{M,n}$ before arriving at the R_x .

The TV Euclidean distance $d_{M,n}^T(t)$ between the transmitter T_x and the n th moving scatterer $S_{M,n}$ is expressed in terms of the TV position of $S_{M,n}$ and the fixed position of T_x by

$$d_{M,n}^T(t) = \sqrt{(x_{M,n}(t) - x^T)^2 + (y_{M,n}(t) - y^T)^2 + (z_{M,n}(t) - z^T)^2}. \quad (\text{D.1})$$

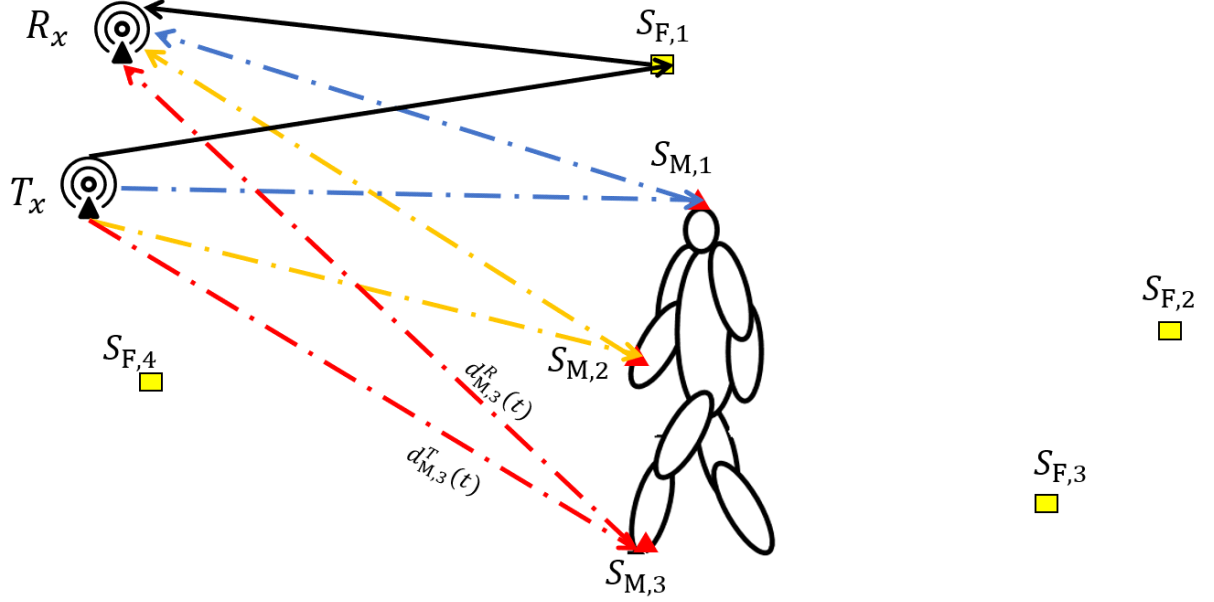


Figure D.1: Propagation scenario consisting of a fixed transmitter T_x , fixed receiver R_x , a moving person modelled by a cluster of \mathcal{N} moving scatterers $S_{M,n}$, and \mathcal{M} fixed scatterers $S_{F,m}$.

Similarly, the Euclidean distance $d_{M,n}^R(t)$ between the receiver R_x and the n th moving scatterer $S_{M,n}$ is given by

$$d_{M,n}^R(t) = \sqrt{(x_{M,n}(t) - x^R)^2 + (y_{M,n}(t) - y^R)^2 + (z_{M,n}(t) - z^R)^2}. \quad (\text{D.2})$$

Using the expressions in (D.1) and (D.2), the total TV propagation delay $\tau_{M,n}(t)$ of the wave travelled from T_x via $S_{M,n}$ to R_x is determined by

$$\tau_{M,n}(t) = \frac{d_{M,n}^T(t) + d_{M,n}^R(t)}{c_0} \quad (\text{D.3})$$

where the parameter c_0 indicates the speed of light.

The complex TV CTF of the 3D non-stationary F2F channel model can be expressed as

$$H(t, \Delta f^{(q)}) = \sum_{n=1}^{\mathcal{N}} c_{M,n}^{(q)}(t) e^{j[\theta_{M,n} - 2\pi(f_0 + \Delta f^{(q)})\tau_{M,n}(t)]} + \sum_{m=1}^{\mathcal{M}} c_{F,m} e^{j[\theta_{F,m} - 2\pi(f_0 + \Delta f^{(q)})\tau_{F,m}]}. \quad (\text{D.4})$$

The parameter $\Delta f^{(q)}$ in (D.4) denotes the subcarrier frequency, which is associated with the q th subcarrier according to

$$\Delta f^{(q)} = q \cdot \Delta \quad (\text{D.5})$$

for $q = -28, -26, \dots, -2, -1, 1, 3, \dots, 27, 28$. The parameter Δ in (D.5) designates the difference between the subcarrier frequencies, which has a constant value of 312.5 kHz [11]. The first term in (D.4) denotes the sum of multipath components corresponding to the \mathcal{N} moving scatterers. Each component of the first term in (D.4) is characterized by a constant phase shift $\theta_{M,n}$, a TV propagation delay $\tau_{M,n}(t)$, and a TV path gain $c_{M,n}^{(q)}(t)$, which are associated with the n th moving scatterer $S_{M,n}$. The TV path gain $c_{M,n}^{(q)}(t)$ depends on the gains of T_x and R_x antennas, the propagation distances $d_{M,n}^T(t)$ and $d_{M,n}^R(t)$, the transmission power, the wavelength of the q th subcarrier $c_0/(f_0 + \Delta f^{(q)})$ [18], and the radar cross-section [19]. The second term in (D.4) denotes the sum of multipath components of the \mathcal{M} fixed scatterers. Each component corresponding to the m th fixed scatterer is characterized by a path gain $c_{F,m}$ and a phase shift $\theta_{F,m}$ due to the interaction with the fixed scatterer. In the simulation, the phases $\theta_{M,n}$ and $\theta_{F,m}$ are the outcomes of identically and independently distributed random variables with a uniform distribution over $-\pi$ and π [20, P. 36].

The Doppler shift $f_n^{(q)}(t)$ associated with the q th subcarrier caused by the n th moving scatterers can be expressed using the relationship $f_n^{(q)}(t) = -(f_0 + \Delta f^{(q)})\dot{\tau}_{M,n}(t)$, which can be found in [21, Eq. (22)] as

$$f_n^{(q)}(t) = -f_{n,\max}^{(q)}(t)\gamma_n(t). \quad (\text{D.6})$$

The function $f_{n,\max}^{(q)}(t)$ denotes the maximum Doppler shift of the q th subcarrier.

$$f_{n,\max}^{(q)}(t) = \frac{(f_0 + \Delta f^{(q)})v_n(t)}{c_0} \quad (\text{D.7})$$

and $\gamma_n(t)$ is given by

$$\begin{aligned} \gamma_n(t) = \cos(\beta_{v_n}(t)) & \left[\cos(\beta_n^T(t)) \cos(\alpha_n^T(t) - \alpha_{v_n}(t)) + \cos(\beta_n^R(t)) \cos(\alpha_{v_n}(t) - \alpha_n^R(t)) \right] \\ & + \sin(\beta_{v_n}(t)) \left[\sin(\beta_n^T(t)) + \sin(\beta_n^R(t)) \right]. \end{aligned} \quad (\text{D.8})$$

The functions $v_n(t)$, $\beta_{v_n}(t)$, $\alpha_{v_n}(t)$, $\alpha_n^T(t)$, $\beta_n^T(t)$, $\alpha_n^R(t)$, and $\beta_n^R(t)$ in (D.7) and (D.8) designate the TV speed of the n th moving scatterer, the TV elevation angle of motion (EAOM), the TV azimuth angle of motion (AAOM), the TV azimuth angle of departure (AAOD), the TV elevation angle of departure (EAOD), the TV azimuth angle of arrival (AAOA), and the TV elevation angle of arrival (EAOA), respectively. More details about these expressions can be found in [22]. The proof of the relationship between the Doppler frequency $f_n^{(q)}(t)$ and the propagation delay $\tau_{M,n}(t)$ can be found in [21]. Note that the function $\gamma_n(t)$ scales the maximum Doppler shift $f_{n,\max}^{(q)}(t)$. The function can be positive or negative depending on the movement of the moving scatterer $S_{M,n}$ relative to the T_x and R_x . If the moving scatterer $S_{M,n}$ moves away from T_x and R_x , its corresponding TV propagation delay $\tau_{M,n}(t)$ increases, i.e., its rate of change with respect to time $\dot{\tau}_{M,n}(t)$ and $\gamma_n(t)$ have positive values.

Hence, according to (D.6), the Doppler frequency $f_n^{(q)}(t)$ has negative values. If the moving scatterer $S_{M,n}$ moves towards T_x and R_x , its corresponding TV propagation delay $\tau_{M,n}(t)$ decreases, and thus, its rate of change with respect to time $\dot{\tau}_{M,n}(t)$ and $\gamma_n(t)$ have negative values. Hence, according to (D.6), the Doppler frequency $f_n^{(q)}(t)$ is larger than zero. The TV mean Doppler shift $B_{f^{(q)}}^{(1)}(t)$ of the presented model in (D.4), associated with the q th subcarrier, can be computed in terms of the path gains $c_{M,n}^{(q)}(t)$ and $c_{F,m}$, and the Doppler frequency $f_n^{(q)}(t)$ as [21]

$$B_{f^{(q)}}^{(1)}(t) = \frac{\sum_{n=1}^{\mathcal{N}} \left(c_{M,n}^{(q)}(t) \right)^2 f_n^{(q)}(t)}{\sum_{n=1}^{\mathcal{N}} \left(c_{M,n}^{(q)}(t) \right)^2 + \sum_{m=1}^{\mathcal{M}} c_{F,m}^2}. \quad (\text{D.9})$$

The expression in (D.9) is the first-order spectral moment which provides the average Doppler shift of the model presented in (D.4) as a sum of the Doppler shifts $f_n^{(q)}(t)$ caused by the moving scatterers $S_{M,n}$ multiplied by their corresponding path gains $c_{M,n}^{(q)}(t)$ and normalized by the sum of the squared path gains of the fixed and moving scatterers. Note that the mean Doppler shift $B_{f^{(q)}}^{(1)}(t)$ in (D.9) is influenced by the path gains of the moving scatterers $c_{M,n}^{(q)}(t)$ and those corresponding to the fixed scatterers $c_{F,m}$. If the path gains of the fixed scatterers $c_{F,m}$ have high values in comparison to those of the moving scatterers $c_{M,n}^{(q)}(t)$, the TV mean Doppler shift $B_{f^{(q)}}^{(1)}(t)$ in (D.9) has small values that approach zero. This can happen in practice if the person moves too far from T_x/R_x . For measured channels, the expression in (D.9) cannot be used, but there is an alternative to estimate it by utilizing the spectrogram, which will be discussed in the next section.

D.3 Spectrogram of the CTF

To compute the spectrogram, an even and positive window function is needed. In this paper, we used the Gaussian window function $w(t)$ given by

$$w(t) = \frac{1}{\sqrt{\sigma_w \sqrt{\pi}}} e^{-\frac{t^2}{2\sigma_w^2}} \quad (\text{D.10})$$

where σ_w denotes the Gaussian window spread parameter. Choosing the value of such a parameter is a trade-off between the frequency resolution and the time localization. If the window spread σ_w is large, the frequency resolution is high, but the time localization is low, and vice versa. Note that the window function has normalized energy, i.e., $\int_{-\infty}^{\infty} w^2(t) dt = 1$.

After choosing the window function, the spectrogram can be computed in three steps. The first step is to compute the short-time CTF $x^{(q)}(t', t)$ which is obtained by multiplying

the sliding window $w(t' - t)$ with the CTF $H(t', \Delta f^{(q)})$, i.e.,

$$x^{(q)}(t', t) = H(t', \Delta f^{(q)}) w(t' - t) \quad (\text{D.11})$$

where the parameters t' and t designate the running time and the local time, respectively. The second step is to compute the short-time Fourier-transform (STFT) $X^{(q)}(f, t)$ by transforming the running time t' to frequency f . The STFT of $H(t', \Delta f^{(q)})$ associated with the q th subcarrier is given by

$$X^{(q)}(f, t) = \int_{-\infty}^{\infty} x(t', t) e^{-j2\pi f t'} dt' = \sum_{n=1}^{\mathcal{N}} X_{\text{M},n}^{(q)}(f, t) + \sum_{m=1}^{\mathcal{M}} X_{\text{F},m}^{(q)}. \quad (\text{D.12})$$

The first and second terms in (D.12) denote the sum of the STFTs corresponding to the \mathcal{N} moving scatterers and the sum of the STFTs corresponding to the \mathcal{M} fixed scatterers, respectively. The last step is to compute the spectrogram $S_{H^{(q)}}(f, t)$ associated with the q th subcarrier by multiplying the STFT in (D.12) with its complex conjugate, which results in

$$S_{H^{(q)}}(f, t) = |X^{(q)}(f, t)|^2 = S_{H^{(q)}}^{(a)}(f, t) + S_{H^{(q)}}^{(c)}(f, t) \quad (\text{D.13})$$

where the functions $S_{H^{(q)}}^{(a)}(f, t)$ and $S_{H^{(q)}}^{(c)}(f, t)$ indicate the auto-term and the cross-term of the spectrogram, respectively. The auto-term $S_{H^{(q)}}^{(a)}(f, t)$ provides insight into the true TV Doppler power characteristics. It is determined by

$$S_{H^{(q)}}^{(a)}(f, t) = \sum_{n=1}^{\mathcal{N}} \left| X_{\text{M},n}^{(q)}(f, t) \right|^2 + \sum_{m=1}^{\mathcal{M}} \left| X_{\text{F},m}^{(q)} \right|^2. \quad (\text{D.14})$$

The first term in (D.14) denotes the superposition of the auto-terms caused by the \mathcal{N} moving scatterers, whereas the second term in (D.14) designates the sum of the auto-terms corresponding to the \mathcal{M} fixed scatterers, i.e., the auto-term consists of $\mathcal{N} + \mathcal{M}$ components. Each component of the first (second) term in (D.14) has the Doppler power characteristics corresponding to the n th moving (m th fixed) scatterer $S_{\text{M},n}$ ($S_{\text{F},m}$). The cross-term $S_{H^{(q)}}^{(c)}(f, t)$ is expressed by (D.15), which can be found at the top of the next page. This term consists of $(\mathcal{N} + \mathcal{M})(\mathcal{N} + \mathcal{M} - 1)/2$ components. The operators $\{\cdot\}^*$ and $\Re\{\cdot\}$ represent the conjugate and the real value operators, respectively. This cross-term in (D.15) represents the undesired spectral interference components that reduce the resolution of the spectrogram. The first term of the cross-term $S_{H^{(q)}}^{(c)}(f, t)$ represents the sum of the spectral interference terms between two different moving scatterers, whereas the second term consists of the sum of the spectral interference terms between two different fixed scatterers. The last term in (D.15) denotes the sum of the spectral interference terms between moving and fixed scatterers. An approximate solution of the spectrogram $S_{H^{(q)}}(f, t)$ of the channel model when using a Gaussian window can be found in [22] by approximating the Doppler frequencies $f_n^{(q)}(t)$ into linear piecewise

$$\begin{aligned}
 S_{H^{(q)}}^{(c)}(f, t) = & 2\Re \left[\sum_{n=1}^{\mathcal{N}-1} \sum_{i=n+1}^{\mathcal{N}} X_{M,n}^{(q)}(f, t) X_{M,i}^{*(q)}(f, t) + \sum_{m=1}^{\mathcal{M}-1} \sum_{i=m+1}^{\mathcal{M}} X_{F,m}^{(q)} X_{F,i}^{*(q)} \right. \\
 & \left. + \sum_{n=1}^{\mathcal{N}} \sum_{i=1}^{\mathcal{M}} X_{M,n}^{(q)}(f, t) X_{F,i}^{*(q)} \right] \tag{D.15}
 \end{aligned}$$

functions. In theory, the cross-term can be eliminated by averaging the spectrogram $S_{H^{(q)}}(f, t)$ over the random phases $\theta_{M,n}$ and $\theta_{F,m}$, i.e., $\mathbf{E}\{S_{H^{(q)}}(f, t)\}_{\theta_{M,n}, \theta_{F,m}} = S_{H^{(q)}}^{(a)}(f, t)$. In practice, however, the cross-term cannot be removed because of the limited number of available snapshot measurements.

From the spectrogram $S_{H^{(q)}}(f, t)$, the TV mean Doppler shift can be computed as

$$B_{H^{(q)}}^{(1)}(t) = \frac{\int_{-\infty}^{\infty} f S_{H^{(q)}}(f, t) df}{\int_{-\infty}^{\infty} S_{H^{(q)}}(f, t) df}. \tag{D.16}$$

The expression in (D.16) can be applied to both, simulation and measurements. Note that the expression in (D.16) is influenced by the cross-term $S_{H^{(q)}}(f, t)$. If the auto-term $S_{H^{(q)}}^{(a)}(f, t)$ is used in the simulation instead of the spectrogram $S_{H^{(q)}}(f, t)$, then the TV mean Doppler shifts $B_{H^{(q)}}^{(1)}(t)$ and $B_{f^{(q)}}^{(1)}(t)$ become equal [23] when computing the TV mean Doppler shift in (D.16).

D.4 Experimental Results

In this section, the spectrograms of the measured CSI for different human activities, and their corresponding TV mean Doppler shifts will be explored. The measurement scenario will be discussed first. Then, the steps for calibrating and processing the CSI data will be described. Finally, the measurement results will be discussed.

D.4.1 Measurement Scenario

A pair of horn antennas YE572113-30SMAM from Laird™ were used as T_x and R_x antenna. They had the same location and the same height, which was 0.8 m. A 22-year-old male candidate with a height of 1.8 m and a weight of 76 kg, was asked to perform some activities while collecting the CSI data. Fig. D.2 illustrates the measurement scenario and the locations corresponding to the activities done by the candidate. The candidate was asked to carry out the following activities:

- *Falling away*: The candidate stood 4 m away from the T_x and R_x and fell in their opposite direction onto a 15 cm high mattress.
- *Falling towards*: The candidate stood 4 m away from the T_x and R_x and fell in the direction towards them onto a 15 cm high mattress.
- *Walking away*: The candidate stood a few centimeters away from the T_x and R_x and walked 4 m away from them.
- *Walking towards*: The candidate stood 4 m away from the T_x and R_x and walked towards them until they were reached.
- *Sitting*: The candidate stood 4 m away from the T_x and R_x , facing them and then sat down on a chair.
- *Bending and straightening*: The candidate stood 4 m away from the T_x and R_x , facing them and then bent forward towards them picking an imaginary object from the floor and then straightening up again.

The candidate did not move after finishing each activity.

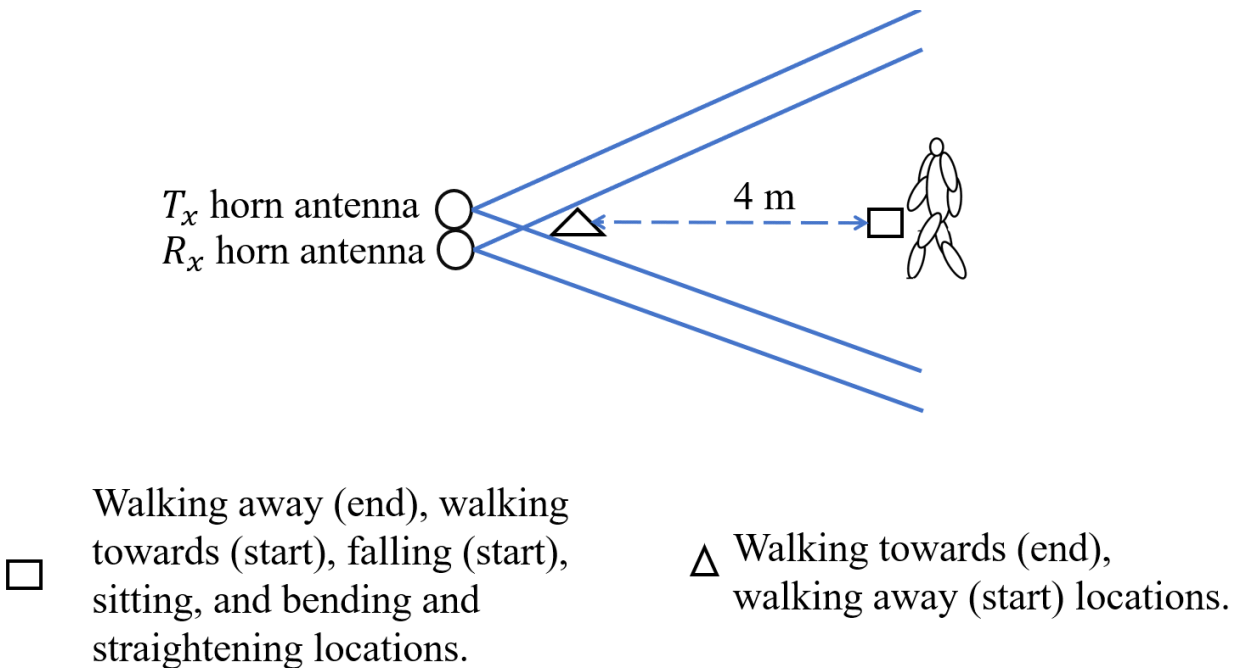


Figure D.2: CSI measurement scenario.

D.4.2 Processing CSI Data

In order to collect RF data, we used two HP Elitebook 6930p laptops equipped with Intel NIC5300. Both laptops had Ubuntu 14.04 LTS operating system, and CSI tool [10] installed. One of the laptops was connected to the T_x antenna, while the other was connected to the R_x antenna. The T_x laptop was working in injector mode, and the R_x laptop was working in monitor mode. Channel 149 was used for recording the CSI data, i.e., the carrier frequency f_0 was chosen to be 5.745 GHz. The bandwidth was set to 20 MHz. The sampling frequency f_s was set to 1 kHz. To overcome the TV phase distortions due to the clock-asynchronization between the T_x and the R_x stations, a B2B connection was employed as illustrated in [17]. To setup the B2B connection, an RF power splitter ZFSC-2-10G+ with one input and two output ports, 4 RF cables 141-1MSM+, and a 30 dB attenuator from Mini-Circuits[®] were utilized. The transmission port of the T_x laptop was connected to the input port of the splitter via an RF cable. For the two output ports of the splitter, one of them was connected to the T_x horn antenna and the other was connected to the attenuator, and then, to one of the RF ports of the R_x laptop using an RF cable. One of the remaining ports of the R_x laptop was used to connect to the R_x horn antenna through an RF cable.

The captured CSI data were stored on two matrices. One of them contained the CTF corresponding to the B2B connection. This matrix had the TV phase distortions. The other matrix contained the CTF corresponding to the R_x antenna and the TV phase distortions. This matrix had channel characteristics and the TV phase distortions. MATLAB 2019b was used for processing the CSI data. The matrix corresponding to the R_x antenna was divided by the matrix corresponding to the B2B connection in elementwise form and stored in a new matrix. This new matrix contained the true micro-Doppler (TV Doppler power) characteristics of the recorded CSI.

Before computing the spectrogram, the CSI matrix containing the true TV Doppler power characteristics was filtered by using a highpass equiripple filter to reduce the effect of the fixed scatterers. Then, we took the sum of the CTF over the subcarriers as follows:

$$\mu(t) = \sum_q H(t, \Delta f^{(q)}). \quad (\text{D.16})$$

This was done for better visualization as it reduces the background noise of the spectrogram. Finally, we computed the spectrogram $S_\mu(f, t)$ of $\mu(t)$, using the same steps as in Section D.3. The window spread parameter σ_w was set to 0.05 s.

D.4.3 Demonstration of the Results

Figs. D.3(a)–D.3(f) exhibit the spectrograms $S_\mu(f, t)$ corresponding to the falling away, falling towards, walking away, walking towards, sitting, and bending and straightening activities of the candidate. For the spectrogram $S_\mu(f, t)$ of the falling away activity shown in Fig. D.3(a),

the Doppler frequency is negative as the candidate moves away from the T_x and R_x . Hence, the propagation delay $\tau_{M,n}(t)$ increases and its rate of change $\dot{\tau}_{M,n}(t)$ is positive (see (D.3) and (D.6)). The Doppler shift caused by the falling activity of the candidate keeps decreasing until it reaches a value around -120 Hz in Fig. D.3(a). Then, it returns to zero value. Fig. D.3(b) depicts the spectrogram $S_\mu(f, t)$ corresponding to the falling towards activity of the candidate. The Doppler frequency caused by the activity is positive since the candidate moves towards the T_x and R_x , thus the propagation delay $\tau_{M,n}(t)$ decreases and its rate of change $\dot{\tau}_{M,n}(t)$ is negative. The Doppler shift corresponding to the falling activity increases until it reaches a value around 100 Hz, then the value drops to zero as the candidate is not moving after the fall. Note that the fall activities depicted in Figs. D.3(a)–D.3(b) include short time intervals up to 2 s. Figs. D.3(c)–D.3(d) exhibit the spectrogram corresponding to the walking away and walking towards activities of the candidate. These activities consume almost 10 s time intervals. The Doppler shift corresponding to the walking away and walking towards activities reach -40 Hz and 40 Hz, respectively.

Fig. D.3(e) shows the spectrogram corresponding to the sitting activity of the candidate. It is shown that the sitting activity lasts for almost 3 s. The pattern of the spectrogram shown in Fig. D.3(e) is quite similar to that in Fig. D.3(a), but the Doppler shift reaches almost -40 Hz unlike the Doppler shift in Fig. D.3(a), which reaches almost -120 Hz. The spectrogram, which corresponds to bending and straightening, is shown in Fig. D.3(f). During the first interval from $t = 0$ s and $t = 2$ s, the Doppler shift reaches almost 20 Hz as when the candidate bends the back, the head gets closer to the T_x and R_x . Thus, the propagation delay $\tau_{M,n}(t)$ decreases and the Doppler shift is positive. In the second interval, from $t = 2$ s to $t \approx 3$ s, the Doppler shift has almost zero value as the person pauses. Thus, the corresponding propagation delay is time-invariant. During the interval from $t \approx 3$ s to $t = 5$ s, the candidate is straightens the back, the propagation delay increases and the Doppler shift is negative as shown in Fig. D.3(f).

Figs. D.4(a)–D.4(f) depict the TV mean Doppler shifts $B^{(1)}(t)$ corresponding to the falling away, falling towards, walking away, walking towards, sitting, and bending and straightening activities of the candidate. These TV mean Doppler shifts were computed by substituting $S_\mu(f, t)$ in (D.16) instead of $S_{H^{(q)}}(f, t)$. The TV mean Doppler shifts exhibited in Figs. D.4(a)–D.4(f) provide similar patterns to the Doppler frequencies shown in the spectrograms depicted in Figs. D.3(a)–D.3(f), but with different values. This is due to the effect of the fixed scatterers, which is not completely eliminated by the highpass filter, the background noise in the spectrogram, and having multiple moving scatterers (see the definition of the TV mean Doppler shift in Section D.2).

D.5 Conclusion

In this paper, we modelled the CTF of 3D non-stationary F2F channels and the TV Doppler frequency caused by the moving scatterer in terms of the TV speed, the TV AAOM, the TV EAOM, the TV AAOA, the TV EAOA, the TV AAOD, and the TV AAOA. We demonstrated the relationship between the Doppler frequency and the TV propagation delay corresponding to the moving scatterer. We provided the expressions of the spectrogram of the CTF, which consists of the auto-term and the cross-term. We expressed the TV mean Doppler shift by means of the spectrogram. We presented the results of the spectrograms and the TV mean Doppler shifts of the calibrated measured CSI for six human activities. The measurement results showed the possibility of applying deep learning or machine learning algorithms for HAR to the spectrograms or the TV mean Doppler shift of the measured calibrated CSI, which can be collected by using commercial devices. For future work, we recommend the development of a channel simulator fed with realistic trajectories of human activities. Such a simulator will contribute to the development simulation-based HAR systems.

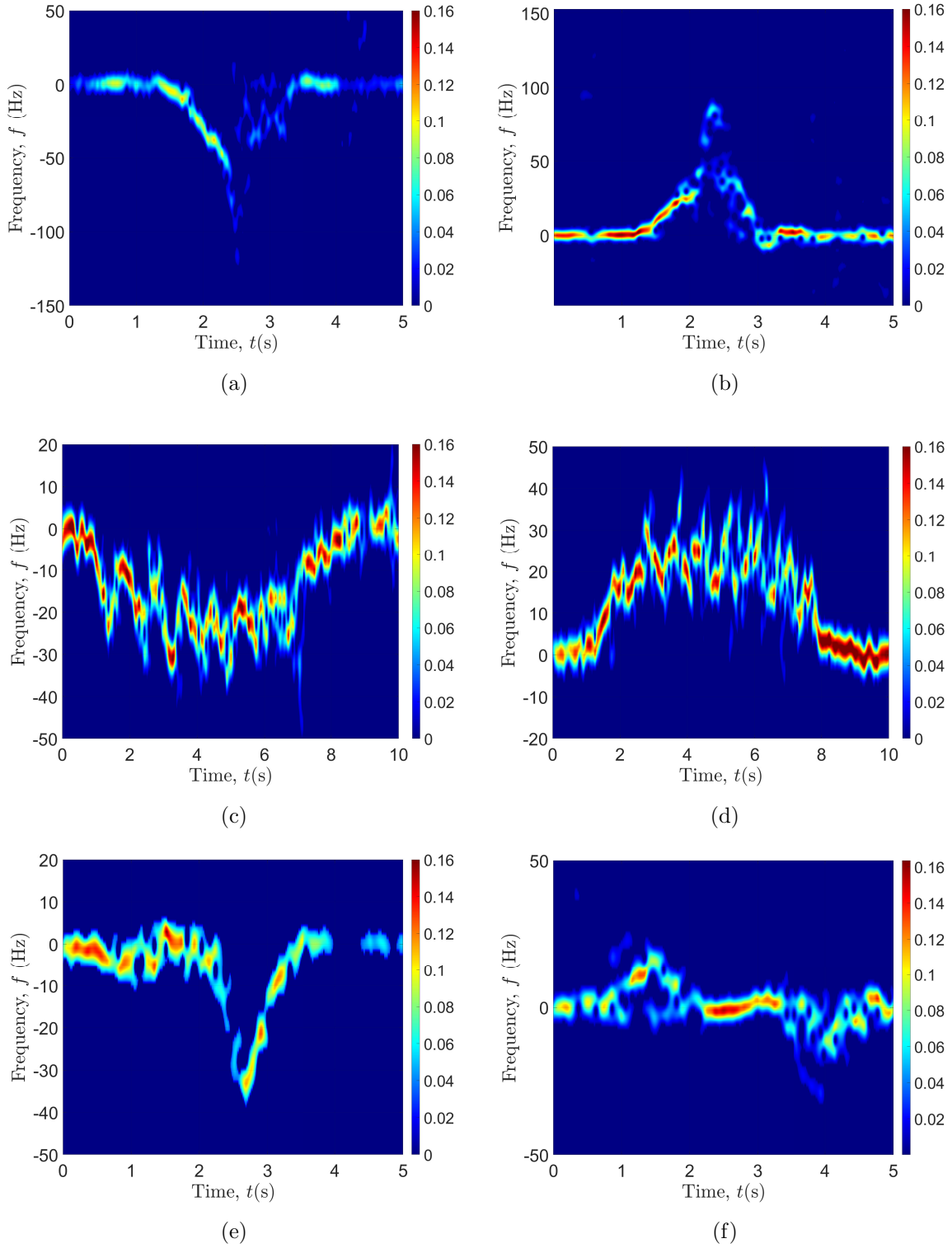
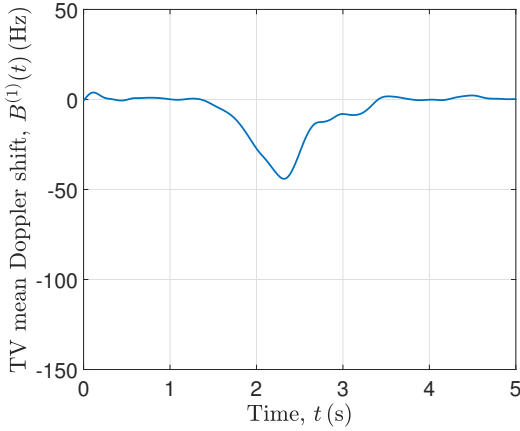
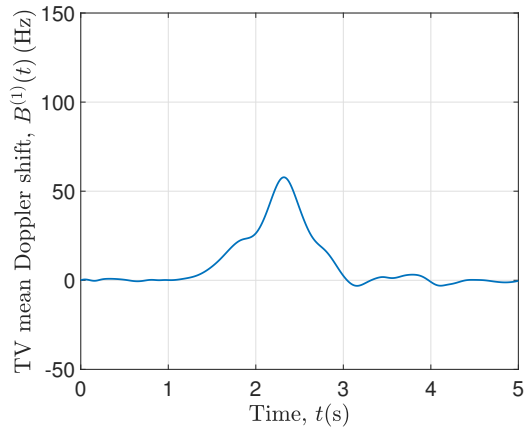


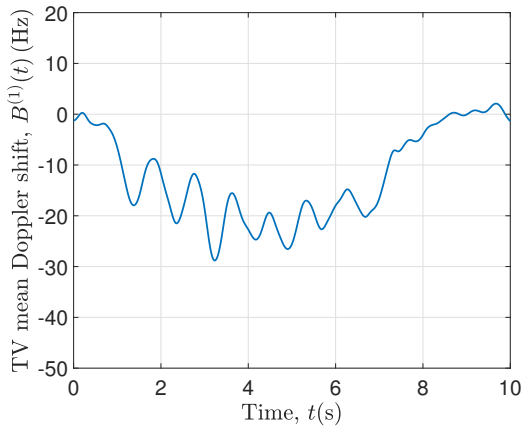
Figure D.3: Spectrograms $S_\mu(f, t)$ of calibrated measured CSI corresponding to the following 6 different human activities (a) falling away, (b) falling towards, (c) walking away, (d) walking towards, (e) sitting, and (f) bending and straightening.



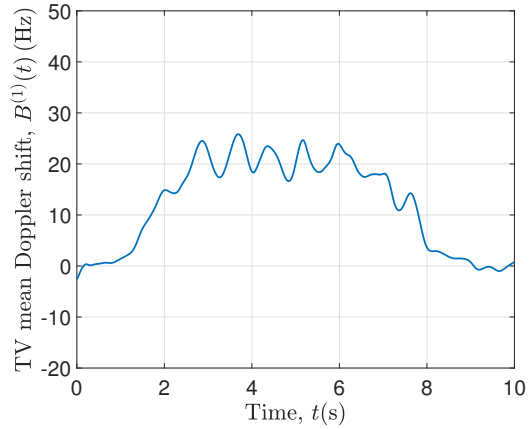
(a)



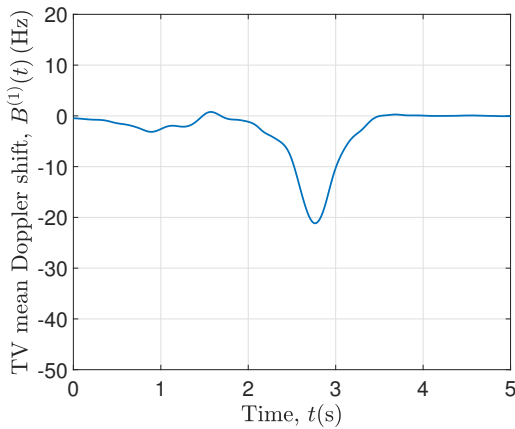
(b)



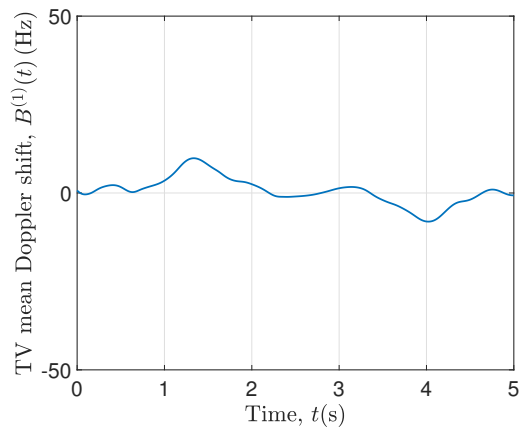
(c)



(d)



(e)



(f)

Figure D.4: TV mean Doppler shifts $B^{(1)}(t)$ of the measured calibrated CSI corresponding to (a) falling away, (b) falling towards, (c) walking away, (d) walking towards, (e) sitting, and (f) bending and straightening activities.

Bibliography

- [1] K. A. Hartholt, R. Lee, E. R. Burns, and E. F. van Beeck, “Mortality from falls among US adults aged 75 years or older, 2000-2016,” *JAMA*, vol. 321, pp. 2131–2133, 06 2019.
- [2] United Nations, Department of Economic and Social Affairs, Population Division , “World population ageing,” 2017. Highlights (ST/ESA/SER.A/408).
- [3] F. Adib, Z. Kabelac, D. Katabi, and R. C. Miller, “3D tracking via body radio reflections,” in *Proc. of the 11th USENIX Conference on Networked Systems Design and Implementation NSDI’14*, (Berkeley, CA, USA), pp. 317–329, USENIX Association, 2014.
- [4] B. Erol and M. G. Amin, “Radar data cube processing for human activity recognition using multi subspace learning,” *IEEE Transactions on Aerospace and Electronic Systems*, pp. 1–1, 2019.
- [5] A. Seifert, A. M. Zoubir, and M. G. Amin, “Detection of gait asymmetry using indoor Doppler radar,” in *2019 IEEE Radar Conference (RadarConf)*, pp. 1–6, April 2019.
- [6] G. A. M, Y. D. Zhang, F. Ahmad, and K. C. D. Ho, “Radar signal processing for elderly fall detection: the future for in-home monitoring,” *IEEE Signal Processing Magazine*, vol. 33, pp. 71–80, Mar. 2016.
- [7] B. Jokanović and M. Amin, “Fall detection using deep learning in range-Doppler radars,” *IEEE Transactions on Aerospace and Electronic Systems*, vol. 54, pp. 180–189, Feb 2018.
- [8] F. Fioranelli, M. Ritchie, S.-Z. Gürbüz, and H. Griffiths, “Feature diversity for optimized human micro-Doppler classification using multistatic radar,” *IEEE Transactions on Aerospace and Electronic Systems*, vol. 53, pp. 640–654, Apr. 2017.
- [9] M. Ritchie and A. M. Jones, “Micro-Doppler gesture recognition using Doppler, time and range based features,” in *2019 IEEE Radar Conference (RadarConf)*, pp. 1–6, April 2019.
- [10] D. Halperin, W. Hu, A. Sheth, and D. Wetherall, “Tool release: gathering 802.11n traces with channel state information,” *ACM SIGCOMM CCR*, vol. 41, p. 53, Jan. 2011.
- [11] “IEEE standard for information technology– local and metropolitan area networks– Specific requirements– Part 11: Wireless LAN medium access control (MAC) and physical layer (PHY) specifications amendment 5: Enhancements for higher throughput,” *IEEE Std 802.11n-2009 (Amendment to IEEE Std 802.11-2007 as amended by IEEE Std 802.11k-2008, IEEE Std 802.11r-2008, IEEE Std 802.11y-2008, and IEEE Std 802.11w-2009)*, pp. 1–565, Oct 2009.

BIBLIOGRAPHY

- [12] M. N. Mahfoudi *et al.*, “Orion: orientation estimation using commodity Wi-Fi,” in *2017 IEEE International Conference on Communications Workshops (ICC Workshops)*, pp. 1233–1238, May 2017.
- [13] M. Kotaru, K. Joshi, D. Bharadia, and S. Katti, “Spotfi: decimeter level localization using WiFi,” *SIGCOMM Comput. Commun. Rev.*, vol. 45, pp. 269–282, August 2015.
- [14] K. Qian *et al.*, “Tuning by turning: Enabling phased array signal processing for WiFi with inertial sensors,” in *IEEE INFOCOM 2016 - The 35th Annual IEEE International Conference on Computer Communications*, pp. 1–9, April 2016.
- [15] W. Wang, A. X. Liu, and M. Shahzad, “Gait recognition using WiFi signals,” in *Proceedings of the 2016 ACM International Joint Conference on Pervasive and Ubiquitous Computing, UbiComp '16*, (New York, NY, USA), pp. 363–373, ACM, 2016.
- [16] S. Sen, B. Radunovic, R. R. Choudhury, and T. Minka, “You are facing the Mona Lisa: spot localization using phy layer information,” in *Proceedings of the 10th International Conference on Mobile Systems, Applications, and Services, MobiSys '12*, (New York, NY, USA), pp. 183–196, ACM, 2012.
- [17] N. Keerativoranan, A. Haniz, K. Saito, and J.-i. Takada, “Mitigation of CSI temporal phase rotation with B2B calibration method for fine-grained motion detection analysis on commodity Wi-Fi devices,” *Sensors*, vol. 18, no. 11, 2018.
- [18] T. K. Sarkar, Zhong Ji, Kyungjung Kim, A. Medouri, and M. Salazar-Palma, “A survey of various propagation models for mobile communication,” *IEEE Antennas and Propagation Magazine*, vol. 45, pp. 51–82, June 2003.
- [19] V. Chen, *The Micro-Doppler Effect in Radar, Second Edition*. Artech House radar library, Artech House, 2019.
- [20] G. L. Stüber, *Principles of Mobile Communications*. Springer Int. Publishing, 4th ed., 2017.
- [21] M. Pätzold and C. A. Gutierrez, “Modelling of non-WSSUS channels with time-variant Doppler and delay characteristics,” in *2018 IEEE Seventh International Conference on Communications and Electronics (ICCE)*, pp. 1–6, Hue, Vietnam, July 2018.
- [22] A. Abdelgawwad and M. Pätzold, “A framework for activity monitoring and fall detection based on the characteristics of indoor channels,” in *IEEE 87th Vehicular Technology Conference (VTC Spring)*, Porto, Portugal, Jun. 2018.

- [23] A. Abdelgawwad and M. Pätzold, “On the influence of walking people on the Doppler spectral characteristics of indoor channels,” in *Proc. 28th IEEE Int. Symp. on Personal, Indoor and Mobile Radio Communications, PIMRC 2017*, Montreal, Canada, Oct. 2017.